# Advancement of Novel Graphene Oxide Embedded Alumina Nickel Composite Coating Developed at Various Current Densities to Evaluate Corrosion Resistance

Usha Pandey [a] and Chhaya Sharma* [b]

In this research, the influence of deposition current density on the properties of nickel-Graphene oxide/alumina coatings produced by electrodeposition was examined. Nickel matrix composite coatings with graphene oxide doped Alumina (GO-Al_2O_3) particles were prepared via electrodeposition. When embedding GO-Al_2O_3 particles in the Ni matrix, remarkable anti-corrosion properties are anticipated due to the outstanding mechanical properties of GO and Al_2O_3. The structure, content, and morphology of GO, GO-Al_2O_3, and coatings deposited at various current densities were determined using X-ray diffraction, Fourier transforms infrared spectroscopy, Field emission Scanning electron microscopy, and energy-dispersive X-ray spectroscopy. GO-doped alumina particles were successfully incorporated into the matrix of nickel, according to the findings. Porosity measurement and cross-sectional thickness were also investigated at various current densities. Potentiodynamic polarization testing and electrochemical impedance spectroscopy were used to study the coatings' corrosion-resistant characteristics. According to the findings, coatings developed at high current densities, such as 30 mA cm^{-2}, are porous and not uniform in nature. Furthermore, at high current densities, the content of GO and Alumina is reduced, resulting in a decrease in mechanical and corrosion resistance. Due to its less porous and uniformly formed coating, 10 mA cm^{-2} was the optimum current density for achieving the most desirable features.

Graphical abstract
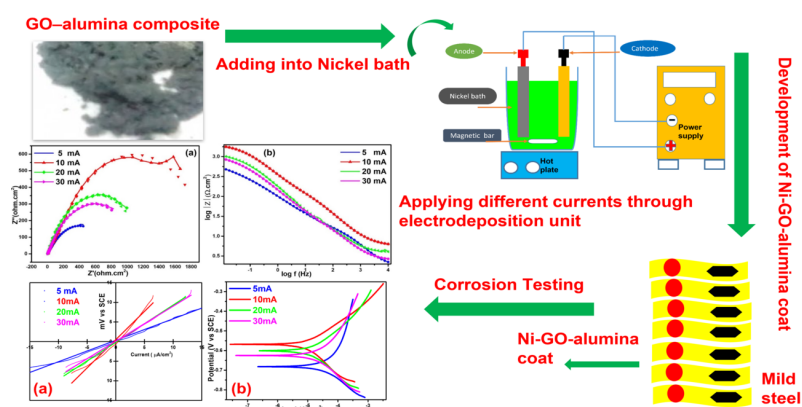
1. Introduction

[a] Department of Applied Science and Engineering, Indian Institute of Technology Roorkee, Saharanpur Campus, Saharanpur, UP 247001, India. [b] Professor, Department of pulp and paper technology Indian Institute of Technology Roorkee, Saharanpur Campus, Saharanpur, UP 247001, India. *Corresponding author: **chhaya.sharma@pt.iitr.ac.in**

Metal matrix coatings incorporated with inert ceramic particles have gotten a lot of interest due to their cost-effectiveness and capability to be prepared by co-deposition in an electroplating bath. Co-deposition of several types of particles (primarily oxides or carbides) and various plating baths are used to form a diverse variety of composite coatings with good characteristics. Coatings comprising well-distributed inert nano-scaled particles in metal matrix exhibit improvement in hardness and corrosion protection properties [1−4]. A matrix of Nickel coatings incorporated with Al_2O_3 particles is frequently utilized in applications that need resistance against wear and endurance, as well as corrosion resistance [5,6]. Due to its various advantageous properties, Al_2O_3 powder is frequently utilized as a second phase to reinforce composite constituents [7].A Watts solution containing powder of alumina is commonly in use for the development of Ni/Al_2O_3 composite coatings using an electrodeposition approach. The number of ceramic particles introduced into the matrix of nickel determines the microstructure and characteristics of the electrodeposited product. The coating's structure and qualities are influenced by particle concentration and distribution, as well as the constituents of the solution used and the parameters of the electroplating bath [2,8]. The current density used in the electrodeposition determines the reinforcement of nanoparticles in a matrix of metal in a bath solution. The morphology and microstructure of composite coatings, which are deposited by using electrodeposition, are influenced by the current density [9]. Various authors have investigated the corrosion resistance of nickel alumina composite coating [10−12]. The effect of current density was analyzed by Anna Goral et al., 2015, who discovered that the coating developed at 5 A/dm^2 had a homogenous dispersion of the ceramic particles, which produced the lowest corrosion current density and the maximum polarization resistance in the measured states [13]. R.K. Saha et al.,2010, discovered that the wt % of Al_2O_3 particles in as-developed coatings increased with current density at first, culminating at 4.3 wt % at 0.01 A/cm^2, and further, the number of particles co-deposited remained constant as current density increased. The highest efficiency of current was attained at a current density of 0.01 A/cm^2 which increased the number of reinforced particles in the coating [14]. Morteza Alizadeh et al., 2019, discovered that the optimum current density for achieving the desired qualities in nickel alumina and molybdenum composite coatings is 4 A/dm^2, where the optimum content of alumina and molybdenum is incorporated, and corrosion resistance was found to be highest[15].

Graphene has recently been studied for anti-corrosive applications in both its pure form and as graphene-integrated metal composite coatings. However, due to the high expense and instrumentation required for producing good-quality graphene in large quantities, commercial usage of graphene for corrosion prevention is still impractical. Graphene oxide (GO), on the other hand, is one of the potential replacements for graphene [16,17]. GO has the same corrosion resistance as graphene and is easily prepared by the chemical oxidation of graphite in large quantities[18−21]. GO has garnered much interest due to its exceptional properties, including a large surface area, ion non-transmissibility, and a surface with many changing functional groups. It offers great potential for anti-corrosion applications [22−27]. Jyotheender et al.,2019, described GO might be advantageous for developing corrosion-resistant coatings since GO is hydrophilic due to the functional groups on it, which allows for better dispersion in the electrolyte [16]. Dong et al.,2017, developed a coating of nickel-graphene oxide (GO) nano-composite using an electro-

brush plating approach, and the effect of GO on the corrosion behavior of the coating as developed was investigated [28]. The corrosion-resistant properties of nanocrystalline Ni and Ni-GO composite coatings generated by pulse electrodeposition utilizing emulsified supercritical carbon dioxide fluids were demonstrated by Wang et al., 2019 [29]. According to Singh et al., 2018, the addition of GO with nickel formed a transfer film on the surface of the stainless steel SS 440c sample, which acted as a lubricant and helped in the increment of wear resistance [30]. Gulam Yasin et al.,2018, demonstrated the electrochemical co-deposition of nickel graphene composite coatings developed at a current density of 9 A/dm^2, which exhibited superior erosion-corrosion resistance. This increased corrosion resistance was observed due to the homogeneous distribution of graphene nano-sheets in the matrix of nickel and its barrier property which gave strength to the coating [31]. Jianqiao Wang et al., 2019, observed that Ni-GO coatings prepared with supercritical-CO$_2$ fluids had a more compact surface, reduced size of the grain, and stronger corrosion protection behavior than pure Ni coatings produced in supercritical-CO$_2$ baths and Ni-GO composite coatings deposited using established methods. The maximum corrosion resistance was found at 6 A/dm^2 current density due to the fine size of the crystal grain and better compactness of the coating without pores and cracks [32].

As a result, in this study, we prepared a Nickel-GO-alumina composite coating, with our interests concentrated on the influence of different current densities on the corrosion behavior of nickel-GO-alumina coatings. Based on the information provided, it can be concluded that no research has been directed to examine the influence of current density on a developed nickel graphene oxide alumina composite coating for corrosion prevention utilizing a simple electrodeposition process. Electrodeposition is a relatively low-cost technology with control over coating thickness and a simple instrument setup, making it appropriate for usage in various applications [14,16]. Because of these benefits, composite coating has been developed using this technology. The composite coating was prepared at varied current densities using a cost-effective electrodeposition technique, and the coatings were characterized using XRD, FE-SEM, FT-ATR, and EDAX. After immersing coated steel samples in a 3.5 % NaCl solution, potentiodynamic polarization, and electrochemical impedance studies were directed to investigate the corrosion-protective nature of the coatings.

2. Material and Methods

2.1 Material and solution

Mild steel (1010) samples for corrosion testing were collected from 'Metal samples' in the United States. **Table 1** shows the components of this collected sample (According to their report), which is also reported in our previous study [17]. Sigma-Aldrich provided the graphite powder (average particle size < 20micrometer) HIMEDIA private limited, India, provided analytical quality sulphuric acid (98%, H_2SO_4), hydrochloric acid (HCl), potassium permanganate ($KMnO_4$), sodium nitrate ($NaNO_3$), and hydrogen peroxide (30 %, H_2O_2) and alumina (80-90 nm size) from Zirox technologies.

2.2 Synthesis of GO and GO-alumina composite

Natural graphite was used to prepare GO using Modified Hummer's method, and graphite powder oxidation takes place vigorously in the presence of H_2SO_4 and $KMnO_4$.The precise

procedure is described [33]. The GO-Al$_2$O$_3$ powder was created by a self-assembling method involving electrostatic contact. In 50 mL of deionized water, 0.1 g of GO was dispersed. In addition, Al$_2$O$_3$ powder (1 g) with a particle size of around 80 nm was added to a 100 ml solution of acetic acid at a concentration of 0.5 mol /L and a pH of 3−4. Both solutions were ultrasonically dispersed for a period of 1 hour. Following that, the suspension of GO was gently added to the Al$_2$O$_3$ while stirring continuously. This solution was then transferred to an oil bath and kept at a temperature of 120 °C for 24 hours. Purified water was used to filter and wash the suspension to remove by-products. During the experiment, the ratio of the mass of GO and Al$_2$O$_3$ in the solution was changed to achieve the desired GO: Al$_2$O$_3$ ratio of 1:10 [34].

Table 1. Components of mild steel (MS 1010)

Components	Wt. %	Components	Wt. %
C	0.08	Mo	0.007
Mn	0.39	Ni	0.023
P	0.015	Cr	0.027
S	0.013	Fe	Remaining
Si	0.013	N	0.0037
Cu	0.03		

* In deionized water, add 35g/L NaCl (Milli Q unit, Merck Millipore, Germany) to make the test solution.

2.3 Development of coating using the electrodeposition approach

The cathode was made of 1 cm^2 mild steel, and the anode was made of a nickel plate. The nickel plate was cleaned with acetone, and the sample of mild steel was refined with emery paper from 100 to 1200 grit. The electrodeposition process was carried out by the DC power supply. The coating was developed under the following conditions: pH ~ 2.5, temperature ~ 45 °C, concentration =1.5 g/L GO-alumina at various current densities (5, 10, 20, and 30 mA cm^{-2}). A diagram of the electrodeposition procedure is presented schematically in **Figure 1**. **Table 2** provides thorough information about the elements contained in the electrolyte bath [35]. For the Nickel ion source, Nickel sulfate is used and Sodium sulfate is used to enhance the rate of deposition, and boric acid is used as a buffer. Therefore, Nickel-GO-alumina composite coating was developed using the solution in **Table 2**.
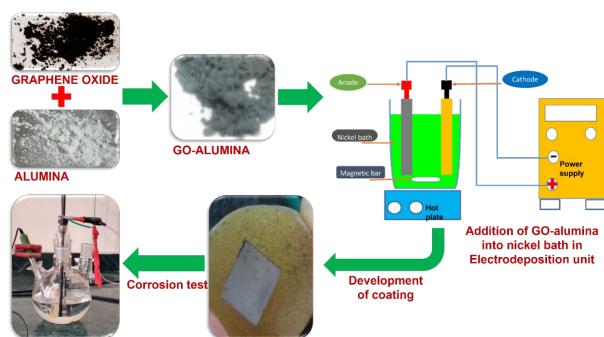

Fig. 1. Schematic diagram of the whole process of development of composite coating and its testing.

2.4 Characterization

A Field Emission Scanning Electron Microscope (FE-SEM) MIRA 3, TESCAN, was used to characterize the composite and the morphology of the as-developed coating sample. The

elements of the coating on mild steel coupons were determined using EDAX (AMETEK, Modal-OCTANE PRIME, USA) and FESEM. Before retaining the sample for SEM, it was coated and sputtered coated with gold with dimensions of 1cm*1cm*1mm. The GO and GO-alumina composites were characterized using FT-ATR (SPECTRUM TWO COMPANY, Perkin−Elmer spectrometer, Singapore), with spectra collected in the range of 500 cm^{-1} to 4000 cm^{-1}. A metallurgical microscope was used to obtain coating porosity on the sample surface (OLYMPUS, BX51, JAPAN). A ferroxyl test (15 g/L NaCl + 25 g/L C$_6$FeK$_4$N$_6$) was performed to determine porosity, which colored the metal sample blue in the presence of iron. As a result, the blue spots may be seen using a metallurgical microscope to evaluate porosity. The structural information of the materials was examined with a Rigaku Ultima IV X-ray diffractometer (XRD) outfitted with Cu k$_\alpha$ radiation (= 0.15406 nm), where a sample was used in powder form. It was drop-cast onto the slide and dried overnight in liquid form. The average crystallite size was calculated using the Debye equation.

Table 2. Constituents of bath solution.

Sample	Electrolyte	Concentration (g/L)
Ni-GO-alumina	NiSO$_4$	26.26
	H$_3$BO$_3$	18.54
	Na$_2$SO$_4$	56.81
	GO-alumina	1.5
	SDS	0.2

2.5 Electrochemical measurements

A sample of area 1 cm^2 embedded in epoxy resin underwent the electrochemical test. Only one face was going to expose to the solution, while the other one was connected to the copper wire electrically. Before performing the electrochemical test, the mild steel was refined with several emery papers of different grades, including 100, 320, 400, 600, 800, 1000, 1200, and 4/0. The samples were degreased with acetone and placed in a 70% alcohol environment under a vacuum [36]. All corrosion experiments were performed according to the American Society for Testing and Materials (ASTM) procedure utilizing a Multichannel potentiostat/galvanostat (AUTO LAB: MAC- 80039, The Netherlands) (A. G3-89). The tests were conducted in standard corrosion cells with an auxiliary electrode of graphite rod, a reference electrode of saturated calomel electrode (SCE), and a working electrode of mild steel with a 1 cm^2 area in a 3.5 % NaCl solution. Linear and Tafel polarization tests were performed to calculate the rate of corrosion. OCP was run for one hour after the mild steel was immersed in a solution of 3.5 % NaCl, and the potential on the y-axis and time on the x-axis was obtained. The sample was polarized with respect to OCP from +250 mV to -250 mV and linear 10 mV OCP at a sweep rate of 0.166 mV/sec for Tafel. Extrapolating the linear component of the cathodic and anodic curves yielded the corrosion current. Linear polarisation curve resistance is obtained from the slope of the linear polarisation curve. This polarisation resistance is converted into corrosion current density using the Stern Geary equation (1) by using the anodic and cathodic slope from the Tafel polarisation curve. The following equation illustrates the anodic and cathodic Tafel slopes, as well as the polarisation resistance R$_p$ [37].

$$I_{corr} = \frac{b_a b_c}{2.303(b_a + b_c).R_p} \dots\dots\dots\dots\dots\dots\dots\dots\dots\dots (1)$$

The corrosion rate was obtained by taking the value of

current density from equation (1) and putting it in equation (2):

$$Corrosion\ rate\ (mpy)$$
$$= 0.13 \times I_{corr}$$
$$\times \frac{EW.}{D} \dots \dots \dots \dots \dots \dots \dots \dots \dots \dots (2)$$

Where EW represents the equivalent weight (g) of mild steel, I_{corr} is the current density ($\mu A/cm^2$), and D is the density in g/cm^3 of the sample [38].

After 60 minutes of dipping the sample in a solution of 3.5 % NaCl, electrochemical impedance spectroscopy (EIS) measurements were performed at OCP with an AC voltage having an amplitude of 0.01 V in the range of frequency between 0.01 Hz to 10 kHz. ZSimpWin software (version 3.21) software was utilized to fit the EIS curve obtained for different samples from the corrosive electrolyte.

3. Results and Discussion

3.1 Characterization of GO-Alumina composite

3.1.1 XRD analysis

Owing to the occurrence of oxygen-containing functional groups, GO has a large and broad diffraction peak at 10.4°, as shown in **Figure 2**. Alumina has a crystalline corundum structure. As shown in the XRD spectra of GO-Al_2O_3 powder, a slight GO peak at 10.4° and no other phases were found besides corundum and GO. This work is also investigated in the previous literature [34].
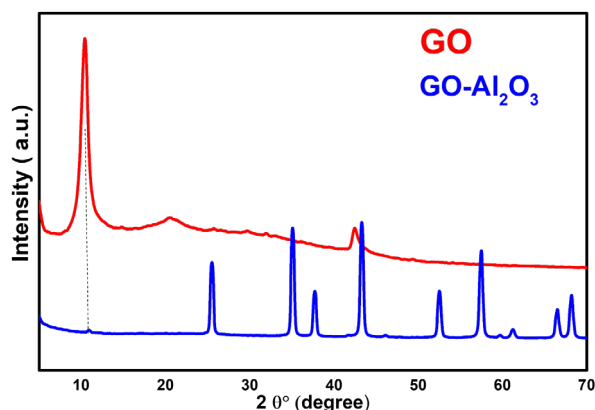
Fig. 2. XRD spectra of GO and GO-alumina composite.

3.1.2 FT-ATR analysis

The Alumina and GO representative groups are depicted in the GO-Al_2O_3 spectrum, as shown in **Figure 3**. At 633 cm^{-1}, GO-Al_2O_3 and Al_2O_3 showed the characteristic Al-O bond absorption. Oxygen-containing functional groups correspond to C-OH stretching vibration, C=C stretching vibration, and C=O stretching vibration of COOH groups at 1230 cm^{-1}, 1567 cm^{-1}, and 1720 cm^{-1}, respectively. The signature peak of the composite is obtained around 1050 cm^{-1}, which correlates to the bonding of Al-O-C, implying that the GO-Al_2O_3 powder induces GO and Al_2O_3 to form chemical bonds.
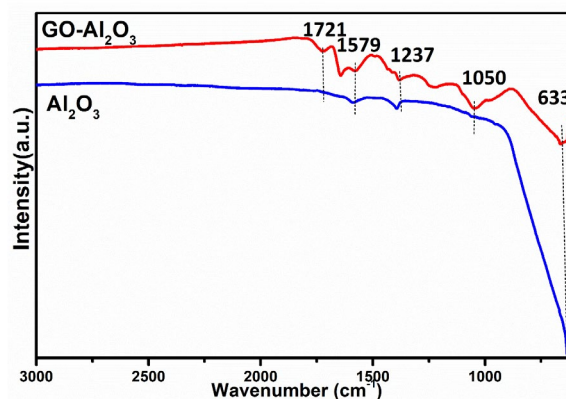
Fig. 3. FT-ATR spectra of GO-alumina composite coating.

3.1.3 Morphology and composition analysis of GO-alumina composite coating

The GO sample has a lamellar structure with wrinkled film morphology, as shown in **Figure 4 (a)**. Because of their enormous specific area, GO sheets also aggregate and show a stacking condition. Different degrees of GO transparency may be seen in the image, and specific dark lines with a lot of contrast suggest wrinkled or folded GO sheets. Most Al_2O_3 nanoparticles were classified as having quasi-spherical shapes, although others had sheet-like or irregular shapes, as seen in **Figure 4 (b)**. In the SEM image of GO-Al_2O_3, the Al_2O_3 nanoparticles are reinforced on the covered structure of GO in **Figure 4 (c)**. The EDS spectra of GO-Al_2O_3 show the existence of C, O, and Al components (**Figure 4(d)**).
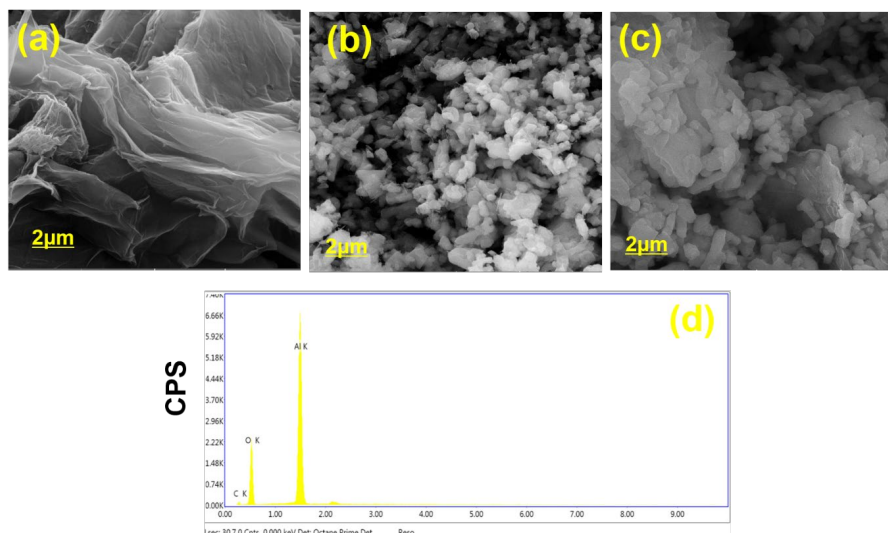
Fig. 4. FE-SEM image of (a) GO; (b) alumina; (c) GO-alumina; and (d) EDAX of GO-alumina.

3.2 Development of coating

3.2.1 *Morphology analysis of as-developed coating at a different current density*

The surface morphology of mild steel before electrodeposition and composite coatings deposited on mild steel at 5, 10, 20, and 30 mA cm^{-2} of current density is shown in **Figure 5**. The morphology of bare mild steel seems to be smooth, as shown in **Figure 5(a),** and this work has been reported earlier [39,40]. The morphology varies from surface to surface, and at low current densities, the coating's morphology is compact and smooth; at high current densities, it becomes less compact and has coarser features. Due to the difference in the conductive nature of the GO-alumina particles and matrix of metal, there is no even dispersion of electric fields across the surface. As a result, the rate of deposition varies by region. The disparity between deposition rates in diverse places is higher at high deposition current densities (such as 20 and 30 mA cm^{-2}), which results in a morphology that is coarse in nature. Furthermore, as the deposition current density rises, there is an increment in the hydrogen bubbles on the surface, resulting in a reduction in compression. It is observed that the surface morphology of the coating at high current densities (30 mA cm^{-2}) develops a spherical shape, as seen in **Figure 5 (d, e)** and also mentioned in one of the previously reported studies [15].
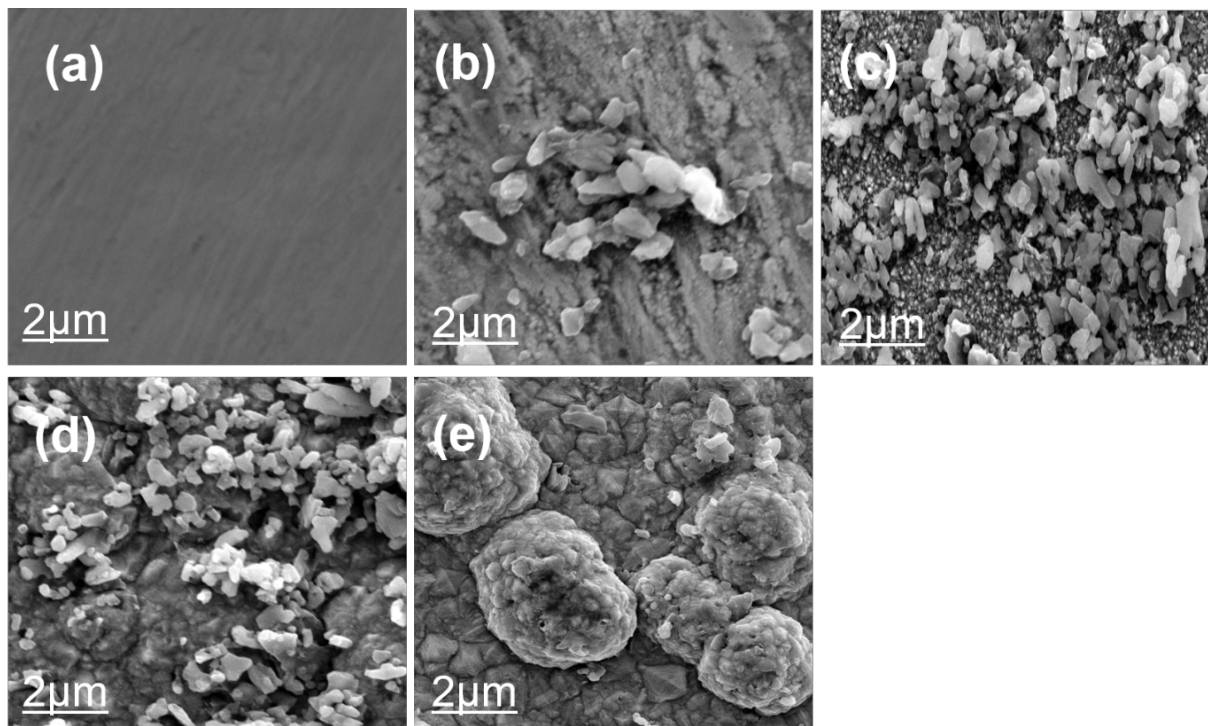

Fig. 5. Morphology analysis of mild steel before (a) and after electrodeposition of Ni-GO-Al$_2$O$_3$ coating at (b) 5; (c)10; (d) 20; and (e) 30 mA cm^{-2} current density.

3.2.2 *Elemental distribution analysis at a different current density*

Elemental maps of Ni-GO/Al$_2$O$_3$ coatings surface treated at various deposition current densities are shown in **Figure 6**. The presence of Ni, GO, and alumina is shown in these images. The GO-alumina particles are evenly spread across the coated surface, as can be seen. It has been found that deposited coatings with a homogeneous particle distribution have improved mechanical and corrosion properties [41,42]. The coatings deposited at 10 mA cm^{-2} contain the greatest GO-alumina particle content and the most uniform particle distribution, as shown in **Figure 6 (b)**. It can be deduced that the coating developed at 10 mA cm^{-2} is the best among all the coatings for corrosion-resistant purposes. A low concentration of GO-doped alumina particles in the coatings resulted from electrodepositing at higher current densities because nickel ions moved more quickly than the GO-doped alumina particles transported by mechanical agitation. On the other hand, nickel ions traveled slowly at low current densities and did not have enough time to bind to GO-alumina particles. Therefore, 10 mA cm^{-2} is the optimum current density to co-deposit nickel and GO-doped alumina homogenously in maximum concentration.

3.2.3 *Cross-sectional morphologies at a different current density*

Figure 7 shows FE-SEM images of the cross-sections of the prepared Ni-GO-Al$_2$O$_3$ nano-composites coatings at various current densities. The particles of GO-doped alumina are well dispersed in developed deposited coatings. The coating thickness was measured around 10, 15, 12, and 27 micrometers for coatings developed at a current density of 5, 10, 20, and 30 mA cm^{-2}, respectively. The optimum thickness is observed for coating developed at 10 mA cm^{-2} of current density because the current density applied is employed for deposition, whereas at higher current densities, the applied current density is squandered in hydrogen evolution, resulting in a decrease in current efficiency. As can be observed, there is a sufficient bond between the deposited coatings at various current densities and their substrates, with no discontinuity amid them. No cracks were observed in the cross-section of these coatings, but at 30 mA cm^{-2}, there are some discontinuities and cracks, which could be attributable to the high nickel ion deposition rate.
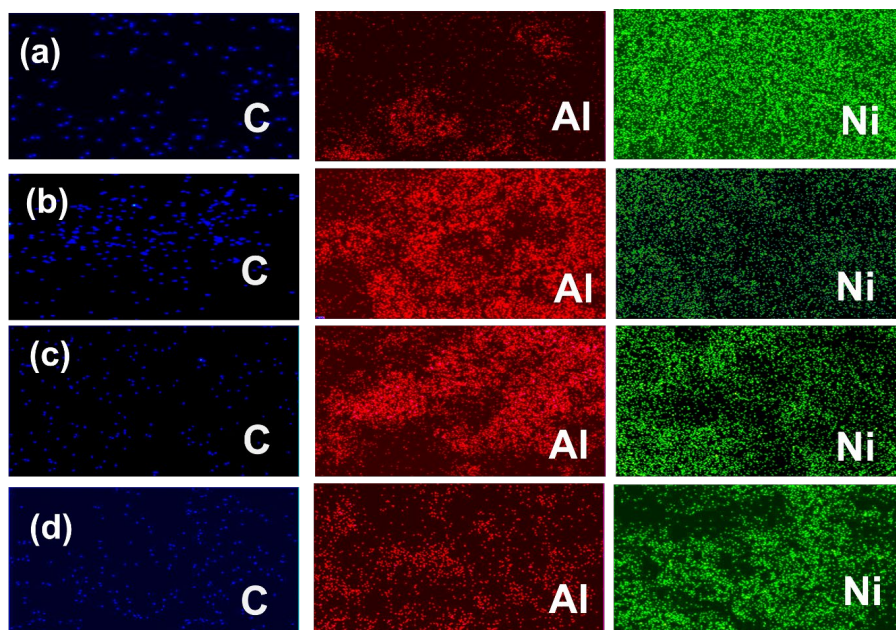
Fig. 6. Elemental distribution maps of as-deposited coatings at different currents density (a) 5; (b)10; (c) 20; and (d) 30 mA cm^{-2}.
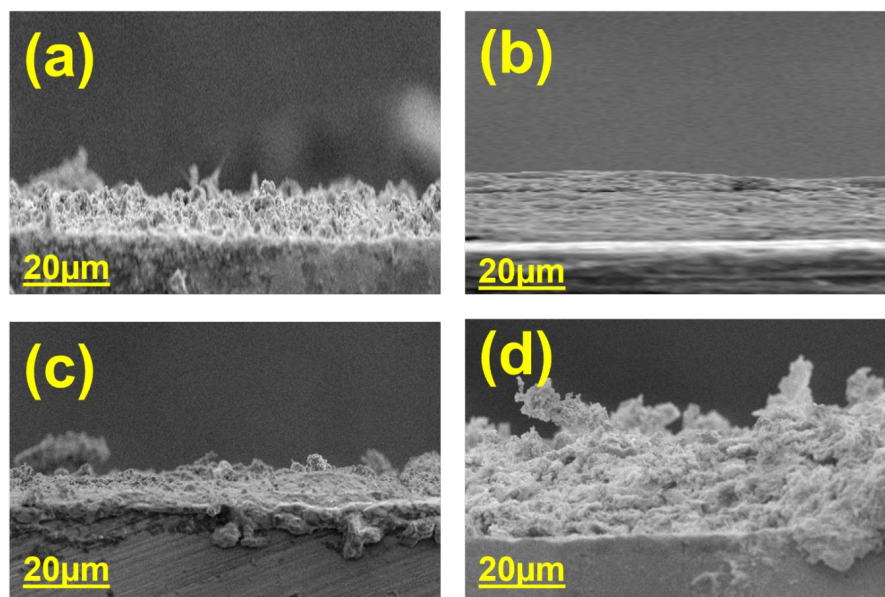

Fig. 7. Cross-sectional thickness at (a) 5 mA; (b) 10 mA; (c) 20 mA; and (d) 30 mA cm^{-2} current density.

3.2. 4 The porosity of the coatings at a different current density

In **Figure 8**, the porosity of as developed coating at different current densities is measured. In **Figure 8 (a) and (d)**, at 5 mA cm^{-2} and 30 mA cm^{-2}, the area having blue color is more compared to coatings developed at 10 and 20 mA cm^{-2} of current density. The least blue spots are found in coating developed at 10 mA cm^{-2} of current density. Hence this can be said that the coating developed at 10 mA cm^{-2} of current density is having least pores. This porosity was detected in the coatings and may be ascribed to hydrogen evolution at the cathode surface, which evidently made its way through the coatings' body and resulted in the observed porosity [14]. Therefore, the porosity has increased while increasing the deposition current density, possibly increasing the formation of hydrogen bubbles at the coating surface. [15].

3.2.5 XRD analysis at a different current density

There are no peaks in the XRD that are related to GO-alumina, as seen in **Figure 9**. This could be owing to a lower level of GO-Alumina composite inclusion in the nickel matrix, which XRD cannot detect. The XRD patterns reveal typical peaks corresponding to (111), (200), and 220 crystallographic planes of pure nickel at 2θ positions 44.508º,51.847º, and 76.8 [43]. The existence of GO-alumina composite in the deposited coating affects the broadening of the peaks, as shown in **Figure 9**. X-ray diffractograms of coatings developed at different current densities are observed in **Figure 9**, where Debye Sherrer's equation (3) was used to determine the average crystallite size of the deposits developed at different current densities.

$$L = \frac{K\lambda}{\beta cos\theta} \dots \dots \dots \dots \dots \dots \dots \dots \dots \dots \dots \dots \dots \dots \dots \dots \dots (3)$$

where λ is the wavelength, β is the full-width half maximum

(FWHM), θ is the diffraction angle, and L is the average crystallite size. **Table 3** lists the values for these parameters. The least size of crystallite of the coatings is confirmed by the broadening of the peak at 10 mA cm^{-2}. The crystallite size was observed as 18.8505, 10.6640, 14.2419, and 16.9161 nm for coatings developed at 5,10,20, and 30 mA cm^{-2} of current density, respectively. In this sense, the size of the crystallite coatings is affected by the current density used in deposition[15].
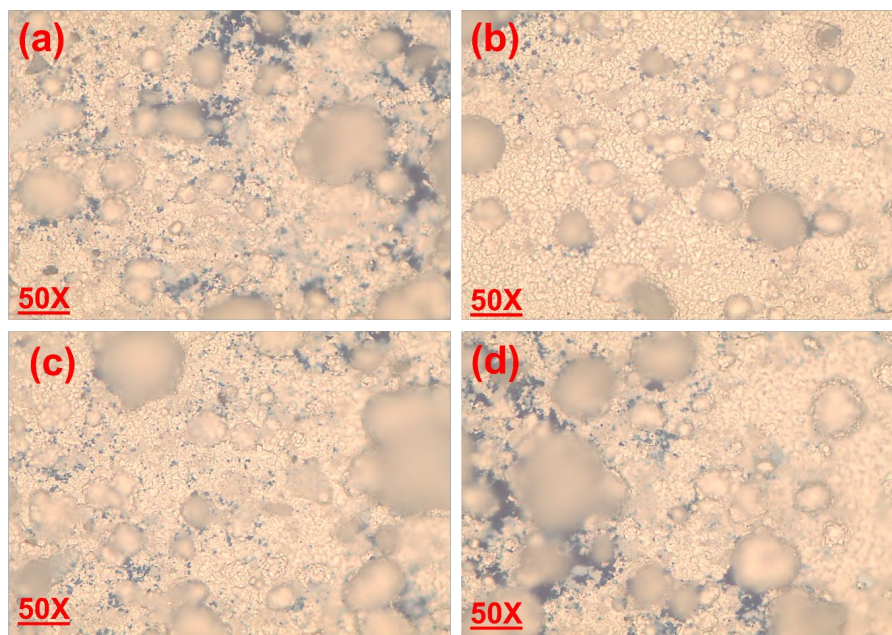

Fig. 8. Optical image of the pores of coating at (a) 5 mA; (b)10 mA; (c) 20 mA; and (d) 30 mA cm^{-2}current density.

Table 3. Scherrer's equation parameters of deposit developed at various current densities.

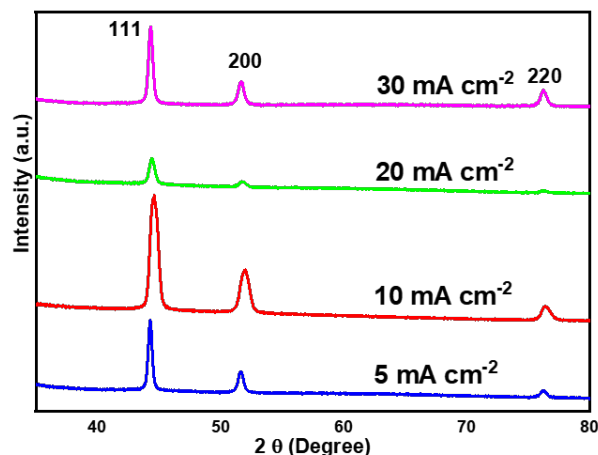| Samples	2θ	FWHM	L	Average L (nm)
5 mA cm^{-2}	44.27	0.3892	22.3635	
	51.63	0.5419	16.3893	18.8505
	76.21	0.572	17.7989	
10 mA cm^{-2}	44.6	0.79418	10.5684	
	51.9	0.95287	9.29316	10.6640
	76.41	0.8342	12.1307	
20 mA cm^{-2}	44.42	0.5254	16.4672	
	51.7	0.60186	14.6879	14.2419
	76.22	0.87301	11.5708	
30 mA cm^{-2}	44.31	0.43925	19.5480	
	51.66	0.58091	15.2082	16.9161
	76.23	0.63215	15.9923	

Fig. 9. XRD spectra of as-deposited Ni-GO-alumina coating at different current densities.
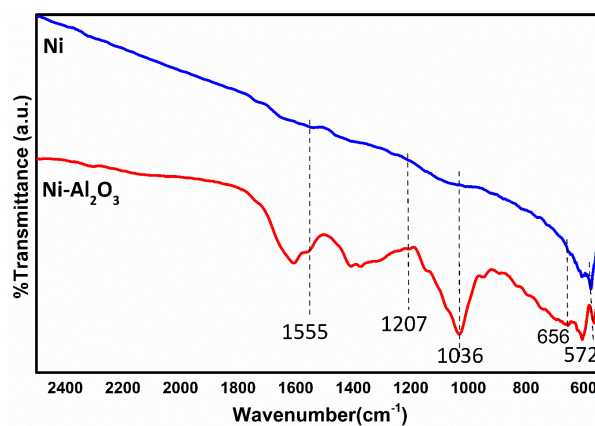
Fig. 10. FT-ATR analysis of the coating developed at 10 mA cm^{-2} current density.

3.2.6 FT-ATR analysis of the as-developed coating

In **Figure 10**, the FT-ATR spectra of Nickel and Nickel-GO-Al$_2$O$_3$ coating are taken. In the Nickel coating, the peak at 572 cm^{-1} is seen, which is the characteristic peak of nickel, and in the nickel-GO-Al$_2$O$_3$ spectra, the peak at 650 cm^{-1} is also seen which is the characteristic peak of alumina. The rest of the all-functional groups of GO are also found, but the intensity was reduced, and the peak at 1720 cm^{-1} has disappeared. All observed peaks confirm the incorporation of GO-alumina composite in the nickel matrix.

3.3 Electrochemical measurements

3.3.1 Electrochemical polarization measurements

Linear polarization resistance (LPR) and Tafel polarization were used to test the corrosion resistance of coatings deposited at various current densities. In a 3.5 % NaCl solution, LPR and Tafel curves of as-coated samples at various current densities were estimated, and the results are presented in **Figure 11 (a, b)**.

The OCP was collected before the linear polarisation test, and the sample was polarised from -10 to +10 mV w.r.t OCP. The slope value is calculated by the E Vs. I curve polarisation resistance. In **Figure 11(a)**, corrosion potential shifts to a positive direction for coating developed at 10 mA cm^{-2} of current density, which is associated with reduced proneness to corrosion. The corrosion prevention nature of as-prepared coatings is demonstrated by estimating corrosion potential and current density decrement. **Table 4** lists all the values received from the Tafel plot and LPR. As a result, it was discovered that $^\beta$a does not equal $^\beta$c, indicating metal corrosion. The dissolution of metal is limited by a decrease in $^\beta$c, which is the least for coating at 10 mA cm^{-2} of current density [16]. In order to calculate the corrosion rate, linear polarisation curves were drawn (**Figure 11(a)**), and the value of R_p was calculated using the linear polarization resistance method. The value of this as acquired R_p is entered into the equation using the Stern Geary approach, and i_{corr} is determined. **Table 4** shows that as compared to others, the corrosion rate in coating developed at 10 mA cm^{-2} of current density is the lowest. From **Figure 11** and **Table 4**, it is observed that the coating deposited at 10 mA cm^{-2} of current density has the lowest corrosion current density among the developed coatings. The coating developed at 30 mA cm^{-2} of

current density has the maximum corrosion current density. It was previously observed that the coating developed at 10 mA cm^{-2} current density contains the maximum GO-alumina composite; it is expected that it should show maximum corrosion resistance. Also, as previously observed, the GO-alumina particle at 10 mA cm^{-2} current density is more uniformly distributed than the coating deposited at 30 mA cm^{-2}. Coating's surface developed at a higher current density has high porosity, which induces the diffusion of Cl$^-$ ions from the corrosive media towards the substrate resulting in a reduction of corrosion resistance.
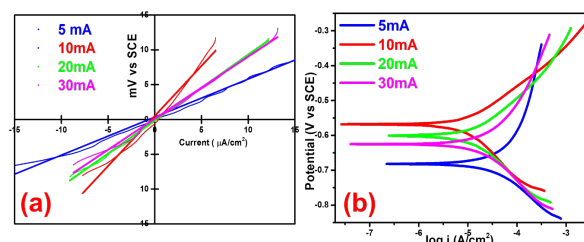

Fig. 11. (a) LPR and (b) Tafel at different current densities (5, 10, 20, and 30 mA cm^{-2}).

3.3.2 Electrochemical Impedance Spectroscopy

In addition to DC polarisation measurement, AC polarisation, i.e., electrochemical impedance spectroscopy (EIS), was utilized to analyze the corrosion process. **Figure 12** shows the Nyquist plot of mild steel-coated samples developed at different current densities in NaCl solution, and in all these cases, the perfect semicircle is not obtained in the impedance curve, as shown in this diagram.

Table 4. Corrosion potential (E_{corr}), anodic and cathodic Tafel slope ($^\beta$a, $^\beta$c), and polarization resistance (R_p) were obtained from polarization curves.

Sample	E_{corr} (mV)	I_{corr} (µAcm^2)	$^\beta$a (mV/dec)	$^\beta$c (mV/dec)	R_p (KΩ.cm^2)	CR (m/Y)
5	-693	104	187	436	0.546	48.09
10	-566	19	155	106	1.436	8.80
20	-600	35.22	159	148	0.946	16.28
30	-625	44.4	177	188	0.891	20.56

Frequency dispersion is caused by electrode surface heterogeneity, which generates this phenomenon [44]. In the Nyquist plot of **Figure 12 (a)**, larger diameter capacitive loops suggest greater corrosion resistance. The EIS curve was fitted to estimate corrosion parameters using the electrochemical equivalent circuits (EEC), as shown in **Figure 12 (c)**, using the Z-SimpWin software. The following are the various circuit elements shown in EEC: R_{coat} and Q_{coat} denoting the impedance which is presented by the as-developed coating and the constant phase element modeling the coated surface, respectively; R_{ct} and Q_{dl} denoting the charge transfer resistance presented at the double layer around the interface of electrode-electrolyte, which is coated electrode and corrosive medium of 3.5 wt % NaCl solution. In order to account for the inhomogeneous nature of the coating surface, a constant phase element was used in place of the capacitor [16]. The EEC model can be used to calculate polarization resistance (R_p), which quantitatively measures corrosion resistance value. R_p is equal to the sum of R_{coat} and R_{ct}. Table 5 also includes R_p values, which show that the R_p values of the coatings grew from coating developed at 5 mA cm^{-2} to coating developed at 10 mA cm^{-2} current density and further decreased from 10 mA cm^{-2} to 20 and 30 mA cm^{-2} coating, respectively. The corrosion-resistant quality of the coatings is associated to the impedance at the low-frequency region of

the bode plots in **Figure 12 (b)**. The coating's impedance is increased in the following order: 5 mA cm^{-2} to 10 mA cm^{-2} and then again reduced. A greater impedance value suggests that the coating is more compact. As a result, the bode plot analysis confirms that the coating developed at 10 mA cm^{-2} of current density has a better corrosion protective layer. This pattern matched that observed in Tafel polarisation studies, which revealed that coating developed at 10 mA cm^{-2} of current density had the best corrosion resistance.

3.3.3 Mechanism of deposition of Ni-GO-alumina coating and its corrosion resistance mechanism

Even though the electrical co-deposition mechanism is not yet fully understood, few models have been put forth recently. All the proposed models share the same fundamental premise: when the particles are captured mechanically or absorbed inside the developing metal film, they reach the Working electrode (WE) via electrophoresis or bath agitation. It has also been suggested in the literature that adsorption of the particle on the WE surface and metal ions reduction adsorbing on the surface of the particle are necessary for the inclusion of the particles into the film. These later mechanisms are challenging to experimentally validate and sustain. The primary mechanism keeping the particles

suspended and facilitating their transportation from the bulk part of the solution to the WE surface is bath agitation [8]. There are five possible sequential steps that make up the co-deposition process: (1) The ionic cloud forming on the particles, (2) convection in the direction of the cathode, (3) diffusion through a hydrodynamic boundary layer, (4) diffusion through a concentration boundary layer, and (5) adsorption at the cathode, where particles are trapped inside the metal deposit and schematic diagram is given in **Figure 13 (a)** [45].
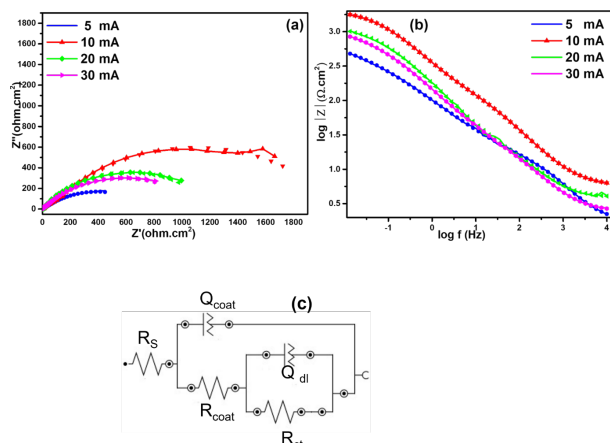

Fig. 12. (a) Nyquist plot; (b) bode plot; and (c) electrochemical equivalent circuit (EEC) used for fitting the EIS data at various current densities (5, 10, 20, and 30 mA cm^{-2}).

It is observed that GO-Al$_2$O$_3$ hybrids have significantly improved the anti-corrosion capabilities at the optimum value of current density. Additionally, the GO-Al$_2$O$_3$ sheet hybrids' corrosion-resistant processes are depicted in **Figure 13 (b)**

The following explanations could be used to explain why GO-Al$_2$O$_3$/nickel improves corrosion protection. The structure of sheets adds an additional layer of barrier to effectively block micro-pores helping in the permeation of electrolyte, which protects the base metal from the attack due to corrosion. Thin hybrids sheet of GO-Al$_2$O$_3$, which is dispersed well in nickel matrix, might inhibit corrosion because they have a substantially greater aspect ratio than stacking of sheets, which may help in improving the corrosion protection performance of composite coatings [46].
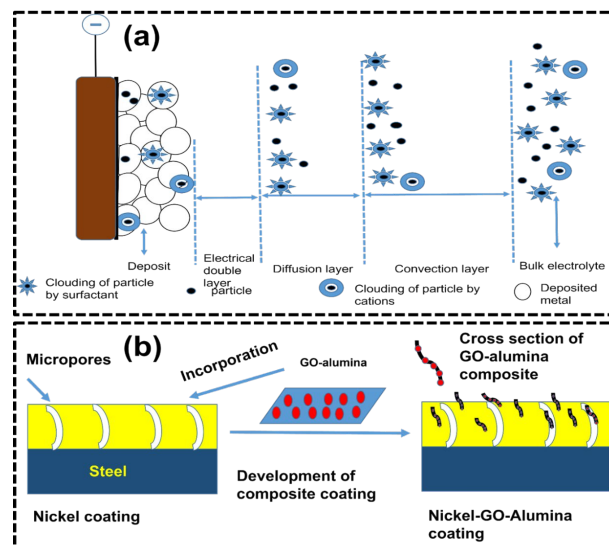

Fig. 13. (a) Mechanisms of particle co-deposition into a metal deposit (b)schematic diagram of corrosion resistance mechanism of Nickel-GO-alumina coating**.**

Table 5. Electrochemical parameters were obtained from the electrochemical equivalent circuit (EEC).

Sample	R_s ($\Omega.cm^2$)	Q_{coat} (S-sec^n)	R_{coat} ($\Omega.cm^2$)	Q_{dl} (S-sec^n)	R_p ($R_{coat}+R_{ct}$) ($\Omega.cm^2$)	$\log|Z|_{10mHz}$ ($\Omega.cm^2$)
5 mA cm^{-2}	1.77	0.0001	12.12	0.003	788.12	2.66
10 mA cm^{-2}	5.5	0.00026	170	0.0006	2110	3.24
20 mA cm^{-2}	3.88	0.0003	18.88	0.001	1229.88	3.01
30mA cm^{-2}	2.39	0.0004	26.8	0.0017	1146.8	2.92

4. Conclusions

Nickel-GO/alumina nano-composite coatings with current densities of 5, 10, 20, and 30 mA cm^{-2} were coated on a mild steel substrate in this investigation. The coatings were studied for their structure, surface morphology, GO-alumina particle distribution, porosity, thickness, and corrosion behavior. The following are the categories for the closing remarks:

1. GO-alumina composite was successfully prepared and characterized by using XRD, FT-ATR, FE-SEM, and EDAX techniques.
2. The nickel matrix was successfully integrated with GO-alumina particles using the electrodeposition technique by applying various deposition current densities (5, 10, 20, and 30 mA cm^{-2}). The current density of the electrodeposition process has influenced the inclusion of GO-Al$_2$O$_3$ nanoparticles in the nickel matrix from a suspension bath.

3. At high deposition current densities, porosity, and cracks increased, which was visualized by an optical microscope and cross-sectional morphology analysis.
4. FE-SEM and EDAX analysis showed that at a current density of 10 mA cm^{-2}, a maximum GO-alumina content was integrated into the matrix, and the GO-alumina particles were evenly dispersed across the coatings' surface.
5. Cross-sectional thickness was increased from 5 to 10 mA cm^{-2} current density, and at a high current density of 30 mA/ cm^2, some cracks and discontinuity were seen which was due to hydrogen evolution.
6. Peak broadening was detected from XRD spectra of as developed coating in 10mA of current density, which showed the least crystalline size of the coating compared to other current densities, and FT-ATR confirmed the incorporation of GO-alumina composite in the nickel matrix.
7. Tafel, LPR, and electrochemical impedance

measurements showed that coatings developed at high current densities (30 mA cm^{-2}) had lower corrosion resistance than those prepared at low current densities (10 mA cm^{-2}). It was established that 10 mA cm^{-2} was the optimum current density for obtaining the desired attributes.

The mechanism of deposition of Ni-GO-alumina composite coating on mild steel substrate using an electrodeposition technique was discussed.

Acknowledgments

Author Contributions

Usha Pandey: Conceptualization, Methodology, Writing – original draft, Visualization, Writing - Review & Editing, Manuscript editing, formatting, Chhaya Sharma: Supervision, Writing - Review, Resources, Investigation, Funding acquisition.

References and Notes

[1] Hovestad, A.; Janssen, L. J. J. *J. Appl. Electrochem.* **1995,** *25*, 519. [Crossref]

[2] Chen, L.; Wang, L.; Zeng, Z.; Xu, T. *Surf. Coatings Technol.* **2006**, *201*, 599. [Crossref]

[3] Gül, H.; Kiliç, F.; Aslan, S.; Alp, A.; Akbulut, H. *Wear* **2009**, *267*, 976. [Crossref]

[4] Wei, X. Y.; Zhu, Z. G.; Prewett, P. D.; Jiang, K. *Microelectron. Eng.* **2007**, *84*, 1256. [Crossref]

[5] Kuo, S. L.; Chen, Y. C.; Ger, M. Der; Hwu, W. H. *Mater. Chem. Phys.* **2004**, *86*, 5. [Crossref]

[6] Aruna, S. T.; Ezhil Selvi, V.; William Grips, V. K.; Rajam, K. S. *J. Appl. Electrochem.* **2011**, *41*, 461. [Crossref]

[7] Wu, G.; Li, N.; Zhou, D.; Mitsuo, K. *Surf. Coatings Technol.* **2004**, *176*, 157. [Crossref]

[8] Corni, I.; Chater, R. J.; Boccaccini, A. R.; Ryan, M. P. *J. Mater. Sci.* **2012**, *47*, 5361. [Crossref]

[9] Bahrololoom, M. E.; Sani, R. *Surf. Coatings Technol.* **2005,** *192*, 154. [Crossref]

[10] Szczygieł, B.; Kołodziej, M. *Electrochim. Acta* **2005**, *50*, 4188. [Crossref]

[11] Szczygieł, B.; Kołodziej, M. *Trans. IMF* **2005**, *83*, 181. [Crossref]

[12] Feng, Q.; Li, T.; Teng, H.; Zhang, X.; Zhang, Y.; Liu, C.; Jin, J. *Surf. Coatings Technol.* **2008**, *202*, 4137. [Crossref]

[13] Góral, A.; Nowak, M.; Berent, K.; Kania, B. *J. Alloys Compd.* **2015**, *615*, S406. [Crossref]

[14] Saha, R. K.; Khan, T. I. *Surf. Coatings* Technol. **2010,** *205*, 890. [Crossref]

[15] Alizadeh, M.; Cheshmpish, *A. Appl. Surf. Sci.* **2019**, *466*, 433. [Crossref]

[16] Jyotheender, K. S.; Srivastava, C. *Compos. Part B Eng.* **2019**, *175*, 107145. [Crossref]

[17] Pandey, U.; Singh, A. K.; Sharma, C. *Synth. Met.* **2022**, *290*, 117135. [Crossref]

[18] Park, J. H.; Park, J. M. *Surf. Coatings Technol.* **2014**, *258*, 62. [Crossref]

[19] Yan, Q.; Zhou, S.; Ma, L.; Wan, S.; Zhu, X. *Surf. Interface Anal.* **2019**, *51*, 152. [Crossref]

[20] Hanafi, N. N.; Sambasevam, K. P.; Arifutzzaman, A.; Rahman, S.; Baharin, S. N. A. *Orbital: Electron. J. Chem.* **2020**, *12*, 205. [Crossref]

[21] de Oliveira, J. P. J.; Vilalva, J. B.; de Sá, A. C.; Paim, L. L. *Orbital: Electron. J. Chem.* **2020**, *12*, 133. [Crossref]

[22] Lai, D.; Chen, P.; Che, C.; Kong, G.; Jiang, Y. *Surf. Interface Anal.* **2021**, *53*, 580. [Crossref]

[23] Mehravar, S.; Fatemi, S.; Komiyama, M. *Surf. Interface Anal.* **2020**, *52*, 547. [Crossref]

[24] Cao, F.; Jiang, P.; Wang, J.; Yan, F. *Surf. Interface Anal.* **2018**, *50*, 667. [Crossref]

[25] Wu, F.; Zhao, W.; Chen, H.; Zeng, Z.; Wu, X.; Xue, Q. *Surf. Interface Anal.* **2017**, *49*, 85. [Crossref]

[26] Ma, L.; Wang, G.; Dai, J. *High Perform. Polym.* **2017**, *29*, 187. [Crossref]

[27] Paredes, J. I.; Villar-Rodil, S.; Martínez-Alonso, A.; Tascon, J. M. D. *Langmuir* **2008**, *24*, 10560. [Crossref]

[28] Qi, S.; Li, X.; Zhang, Z.; Dong, H. *Thin Solid Films* **2017**, *644*, 106. [Crossref]

[29] Wang, J.; Lei, W.; Deng, Y.; Xue, Z.; Qian, H.; Liu, W.; Li, X. *Surf. Coatings Technol.* **2019**, *358*, 765. [Crossref]

[30] Singh, S.; Samanta, S.; Das, A. K.; Sahoo, R. R. *Surfaces and Interfaces* **2018,** *12*, 61. [Crossref]

[31] Yasin, G.; Arif, M.; Shakeel, M.; Dun, Y.; Zuo, Y.; Khan, W. Q.; Tang, Y.; Khan, A.; Nadeem, M. *Adv. Eng. Mater.* **2018**, *20*, 1701166. [Crossref]

[32] Wang, J.; Lei, W.; Deng, Y.; Xue, Z.; Qian, H.; Liu, W.; Li, X. *Surf. Coatings Technol.* **2019**, *358*, 765. [Crossref]

[33] Kruusenberg, I.; Mondal, J.; Matisen, L.; Sammelselg, V.; Tammeveski, K. *Electrochem. Commun.* **2013**, *33*, 18. [Crossref]

[34] Yin, H.; Dai, Q.; Hao, X.; Huang, W.; Wang, X. *Surf. Coatings Technol.* **2018**, 352, 411. [Crossref]

[35] Kumar, C. M. P.; Venkatesha, T. V.; Shabadi, R. *Mater. Res. Bull.* **2013**, *48*, 1477. [Crossref]

[36] Li, H.; Yang, C.; Zhou, E.; Yang, C.; Feng, H.; Jiang, Z.; Xu, D.; Gu, T.; Yang, K. *J. Mater. Sci. Technol.* **2017**, *33*, 1596. [Crossref]

[37] Boudellioua, H.; Hamlaoui, Y.; Tifouti, L.; Pedraza, F. *Appl. Surf. Sci.* **2019**, *473*, 449. [Crossref]

[38] Saricimen, H.; Mohammad, M.; Quddus, A.; Shameem, M.; Barry, M. S. *Cem. Concr. Compos.* **2002**, *24*, 89. [Crossref]

[39] Prajila, M.; Joseph, A. *J. Bio- Tribo-Corrosion* **2017**, *3*, 1. [Crossref]

[40] Boudalia, M.; Fernández-Domene, R. M.; Guo, L.; Echihi, S.; Belghiti, M. E.; Zarrouk, A.; Bellaouchou, A.; Guenbour, A.; García-Antón, J. *Materials (Basel)* **2023**, 16. [Crossref]

[41] Allahyarzadeh, M. H.; Aliofkhazraei, M.; Rouhaghdam,

A. R. S.; Torabinejad, V. *J. Alloys Compd.* **2016**, *666*, 217. **[Crossref]**

[42]   Laszczyńska, A.; Winiarski, J.; Szczygieł, B.; Szczygieł, I. *Appl. Surf. Sci.* **2016**, *369*, 224. **[Crossref]**

[43]   Borkar, T.; Harimkar, S. P. *Surf. Coatings Technol.* **2011**, *205*, 4124. **[Crossref]**

[44]   Migahed, M. A.; Hegazy, M. A.; Al-Sabagh, A. M. *Corros. Sci.* **2012**, *61*, 10. **[Crossref]**

[45]   Low, C. T. J.; Wills, R. G. A.; Walsh, F. C. *Surf. Coatings Technol.* **2006**, *201*, 371. **[Crossref]**

[46]   Yu, Z.; Di, H.; Ma, Y.; Lv, L.; Pan, Y.; Zhang, C.; He, Y. *Appl. Surf. Sci.* **2015,** *351*, 986. **[Crossref]**

How to cite this article